Journal of Materials Chemistry C

ROYAL SOCIETY OF CHEMISTRY

PAPER

View Article Online
View Journal | View Issue

Cite this: J. Mater. Chem. C, 2023, 11, 7662

Efficient down-shifting and up-conversion emission dual-mode in RE^{3+}-doped $NaTbF_4$-based nano-glass ceramics

Javier del-Castillo, Angel Carlos Yanes * and Moisés Cantón-Jara

Received 6th March 2023,
Accepted 5th May 2023

DOI: 10.1039/d3tc00816a

rsc.li/materials-c

Undoped and RE^{3+}-doped (Eu^{3+}, Yb^{3+}) nano-glass ceramics (nGCs) comprising $NaTbF_4$ nanocrystals (NCs) were obtained by thermal treatment of precursor sol–gel glasses. The structural characterization was carried out by X-ray diffraction, transmission electron microscopy and electron dispersive X-ray spectroscopy, which confirm that spherical cubic phase $NaTbF_4$ NCs were precipitated and uniformly distributed in the silica matrix. Additionally, in order to study the local environment of the dopant RE^{3+} ions and their distribution in nGCs, Eu^{3+} ions were considered as a spectroscopic probe. These materials present intense green and red emissions from Tb^{3+} and Eu^{3+} ions, respectively, both by down-shifting from UV-blue excitation, as well as cooperative up-conversion from 980 nm NIR excitation processes. In order to quantify the efficiency of all these emissions, the corresponding quantum yields were measured. Very efficient energy migration from Yb^{3+} to Eu^{3+} through Tb^{3+} ions made it possible to obtain long lived UC red emissions from Eu^{3+} ions, which are very useful in time-gated luminescence techniques. Through time resolved spectra and luminescence decay measurements, the involved energy transfer mechanisms were proposed. All these results allow considering these nGCs as dual-wavelength mode UV/NIR to VIS converter materials, with potential utility in solar cells, w-LEDs and anti-counterfeiting applications.

1 Introduction

Rare-earth (RE^{3+}) based nanostructured materials for photon down-shifting (DS) and up-conversion (UC) processes, from ultraviolet (UV) and near-infrared radiation (NIR), respectively, have been an active field of research in recent years for their diverse and important applications, such as lasers,[1–3] solar cells,[4–6] w-LEDs,[7,8] bio-imaging,[9–12] temperature sensing,[13,14] anti-counterfeiting,[15–19] photocatalysis,[20,21] and so on. Among these materials, transparent RE^{3+}-doped nano-glass ceramics (nGCs) comprising fluoride nanocrystals (NCs) in a robust oxide glassy matrix stand out, for they combine the advantages of the thermal, mechanical and chemical properties of oxide glasses with the low phonon energy of crystalline fluoride environments.[22] Because RE^{3+} dopants are mainly confined in crystalline environments, where the non-radiative quenching of emissions is restricted, they present long excited-state lifetimes and large optical absorption cross-sections, therefore yielding higher efficiencies when compared to the remaining ions in the surrounding glass.[23]

Among RE^{3+} ions, Tb^{3+} and Eu^{3+} are very attractive as DS emitting ions because the high quantum efficiencies related to the large energy gap between the emitting states and the low lying $^7F_{J=0,1,..,7}$ excited states give place to intense green and red emissions in the visible region. Moreover, Tb^{3+} ions have also been proven to be one of the most suitable sensitizers for Eu^{3+} emissions.[24,25] However, the use of both ions as upconverters is very limited because of the inefficient absorption of infrared photons. As it is well known, the most efficient UC systems are based on the energy transfer (ET) between Yb^{3+} and Ho^{3+}, Er^{3+} or Tm^{3+} ions, yielding green, red and blue emissions.[23,26,27] The Yb^{3+} ion is used as a suitable sensitizer because it strongly absorbs NIR radiation at around 980 nm and can efficiently transfer it to these RE^{3+} ions due to their ladder-like energy levels. However, UC from Tb^{3+} and Eu^{3+} ions, without intermediate energy levels resonant with Yb^{3+} ions, is completely different and requires the least efficient cooperative energy transfer (CET) mechanism, where two Yb^{3+} ions that are excited by NIR radiation simultaneously combine and transfer their energies to one of these ions.[28–30] In this regard, it should be noted that Tb^{3+} ions are more interesting candidates to be excited by a cooperative process from Yb^{3+} ions, because in this case the energy transfer is resonant.

Among the fluoride NCs, $NaTbF_4$ is a very attractive optical material. However, it has been poorly researched, and no UC luminescent properties have been reported so far.[31–33] It

Departamento de Física, Universidad de La Laguna, 38200 La Laguna, Tenerife, Spain. E-mail: ayanesh@ull.edu.es

presents a very low-phonon energy ($\sim$350 cm^{-1}) and suitable Tb^{3+} sites that can be easily substituted by other RE^{3+} ions without additional charge compensation. Thus, besides simultaneously serving as constituents of the crystalline lattice, due to the high content of Tb^{3+}, and as activators,[31] Tb^{3+} ions in $NaTbF_4$ NCs can also easily act as sensitizers, strongly absorbing the incident energy and then transferring it to other RE^{3+} ions.[32,33] They can also act as an excellent energy migrator, favoring the ET processes in NCs through the chain $Tb^{3+} \rightarrow (Tb^{3+})_n \rightarrow RE^{3+}$, and providing an enhancement of luminescent properties of the activator ions.[34]

In previous studies, we developed efficient green emitter Yb^{3+}–Tb^{3+} co-doped up-converting systems based on CET that use KYF_4 NCs embedded in silica glasses.[35] We have also explored DS ET from Ce^{3+} to Eu^{3+} ions in Ce^{3+}–Tb^{3+}–Eu^{3+} tri-doped KYF_4 and LaF_3 based nGCs under Ce^{3+} UV excitation, where Tb^{3+} ions act as the bridging ion through which the excitation energy was transferred from the Ce^{3+} sensitizers to the Eu^{3+} activator ions.[7,36] Thus, in $NaTbF_4$ based nGCs, one could expect NIR UC based on $Yb^{3+} \rightarrow Tb^{3+} \rightarrow Eu^{3+}$ ET to be more efficient than the direct cooperative sensitization process between Yb^{3+} and Eu^{3+} ions. They can also be a good alternative for conventional red emitting Ho^{3+}/Er^{3+}-based UC systems, with the additional merit of their longer lifetime and a potential utility in applications that require the use of a time-gated technique.[37]

In the present work, we have successfully obtained a series of nGCs based on cubic $NaTbF_4$ NCs undoped and doped with Yb^{3+} and/or Eu^{3+} ions *via* the sol–gel method and subsequent heat treatments, that combine both DS and UC luminescence from identical RE^{3+} ions. Their morphological and structural characteristics were studied by means of X-ray powder diffraction (XRD), transmission electron microscopy (TEM) and energy dispersive X-ray spectroscopy (EDS) measurements, and also by using the activator Eu^{3+} ion as an optical probe to study the local environment of the RE^{3+} dopant ions in the nGCs. Very efficient green or red emissions were obtained through DS and cooperative UC (CUC) mechanisms, where Tb^{3+} ions acted as the activator, as the sensitizer to Eu^{3+} emissions, or as the energy migrator transferring the absorbed energy from Yb^{3+} to Eu^{3+} ions. The corresponding properties and mechanisms of all emissions were studied and are discussed in detail.

2 Experimental section

2.1 Materials

Materials used, of analytical grade and without further purification, were purchased from Sigma-Aldrich and Merck: TEOS (99.999%), sodium acetate (99.995%), terbium acetate (99.9%), europium acetate (99.9%), ytterbium acetate (99.95%), trifluoracetic acid (>99%), ethanol (>99%, Merck), acetic acid (>99%, Merck), and deionized water (Sigma-Aldrich).

2.2 Synthesis

Silica glasses with composition $95SiO_2$–$5NaTb_{(1-x-y)}Eu_xYb_yF_4$ in mol% (x = 0, 0.02 and y = 0, 0.1 or 0.2) were obtained by a sol–gel method as it was described by J. Méndez-Ramos *et al.*[27] Tetraethyl orthosilicate (TEOS) was used as the source of SiO_2 and hydrolyzed for 1 hour at room temperature with a solution of ethanol, deionized H_2O and acetic acid as the catalyst. The required quantities of $Na(CH_3COO)$, $Tb(CH_3COO)_3xH_2O$, $Eu(CH_3COO)_3xH_2O$ and $Yb(CH_3COO)_3xH_2O$, dissolved in a trifluoracetic acid aqueous solution, were slowly added dropwise into the above solution and vigorously stirred for 1 h to obtain a homogeneous solution. The resulting solution, in a sealed container at 35 °C, gave rise to transparent gels after 10 days. Through slow evaporation, these gels were dried for 6 weeks. Finally, these dried gels were thermally treated under an air atmosphere at 650 °C, the optimal temperature to achieve a stiff glass network and the controlled precipitation of $NaTbF_4$ NCs required to produce nGCs without loss of transparency. Silica glass doped with 2 mol% of Eu^{3+} was obtained using a similar procedure for comparison purposes.

2.3. Characterization

The XRD measurements were carried out with a Philips Panalytical X'Pert Pro diffractometer (with a primary monochromator, a $Cu_{K\alpha1}$ radiation source (λ = 1.5406 Å), and an X'Celerator detector). XRD patterns were recorded with a step of 0.016° in the 2θ angular range (15–80°) for 30 min. As an internal standard diffraction pattern, to calibrate the parameters of the instrumental profile, LaB_6 was used. Moreover, TEM images and EDS measurements were performed using a transmission electron microscope (JEOL-2100F), with a field emission gun, operating at 200 kV and a point-to-point resolution of 0.24 nm. The analyzed samples were obtained by dispersing fine powder (after grinding the nGCs) in acetone and finally dropping them onto carbon-coated copper grids.

Steady state and time-resolved photoluminescence (PL) measurements were carried out with a PTI spectrometer controlled using Felix32 software, which was equipped with a 75 W xenon arc and flash lamps as excitation sources, whose beams passed through an excitation 0.2 m monochromator and was detected with a 0.2 m emission monochromator, and provided with an R928 Hamamatsu PMT. A tunable pulsed laser (EKSPLA-NT342-3-UVE-6 ns-10 Hz) optical parametric oscillator (OPO), pumped by the third harmonic wavelength at 355 nm of a Q-switched YAG:Nd laser, tuned to 483 nm in order to excite the studied samples, was used to measure the emission increase and decay times. Detection was registered by using an R928 photomultiplier and a digital oscilloscope (Keysight DSOX 2024A).

Photoluminescence quantum yield (PLQY) and UC quantum yield (UCQY) were measured with an Edinburgh spectrofluorimeter FLS 1000 equipped with a 15 cm integration sphere SC30, through the expression $\eta = \int L_S / \int E_R - E_S$, where L_S is the area of the emission spectrum, while E_R and E_S are the corresponding areas for the excitation light source, without and with the sample, respectively. The excitation wavelength was 351 nm by using a Xe lamp (150 W) and 980 nm using a laser diode with a power density of 100 W cm^{-2}, as excitation

sources. The equipment was calibrated with [Eu(phen)(tta)$_3$] with a quantum yield of 69%.

For UC measurements, a 980 nm commercial laser diode with a pump power of up to 300 mW was used, along with a 50 mm focal lens to concentrate the incident radiation onto the nGCs. Detection was carried out with a 0.2 m emission monochromator equipped with an R928 Hamamatsu PMT. The power density can be roughly estimated from the beam diameter (2 mm), the incident laser excitation pump power and the lens focal length. All measurements were taken at room temperature and corrected by the instrumental response of the equipment. Additionally, a CCD digital camera was used to obtain color photographs of transparent nGCs.

3 Results and discussion

3.1 Structural characterization

Fig. 1 shows the XRD patterns of a precursor glass and the nGCs with compositions 95SiO_2–5$NaTbF_4$, 95SiO_2–5$NaTb_{0.98}Eu_{0.02}F_4$ and 95SiO_2–5$NaTb_{0.78}Eu_{0.02}Yb_{0.20}F_4$, heat-treated at 650 °C. In addition, the standard diffraction pattern of cubic $NaTbF_4$ (JCPDS 27-0808) is also included for comparison. On the one hand, the characteristic broad band of SiO_2 in the amorphous state at around 20° (see precursor glass pattern) can be clearly observed together with the superimposed diffraction peaks at 27.6°, 31.8°, 46.0°, 54.2°, 67.1° and 75.3°, which correspond to the precipitation of $NaTbF_4$ NCs in the cubic phase (fluorite structure, space group $Fm\bar{3}m$).[32,34] Moreover, from the diffraction patterns and by using the Scherrer equation, it is possible to determine the size of NCs. Thus, mean sizes of 21.0, 22.2, and 24.4 nm are obtained for the nGCs 95SiO_2–5$NaTbF_4$, 95SiO_2–5$NaTb_{0.98}Eu_{0.02}F_4$ and 95SiO_2–5$NaTb_{0.78}Eu_{0.02}Yb_{0.20}F_4$, respectively, much smaller than those previously obtained by X. Li *et. al.* (around 71 nm), in melt quenching nGCs comprising $NaTbF_4$ NCs.[34]

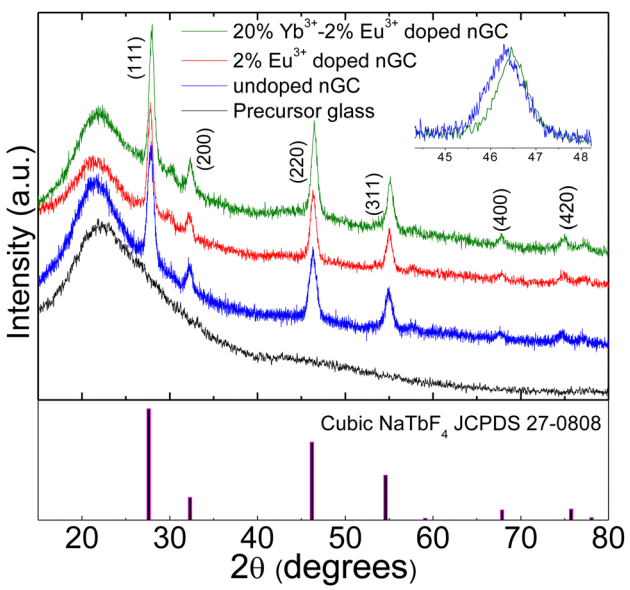

Fig. 1 XRD patterns of precursor glass and nGCs with compositions 95SiO_2–5$NaTbF_4$, 95SiO_2–5$NaTb_{0.98}Eu_{0.02}F_4$ and 95SiO_2–5$NaTb_{0.78}Eu_{0.02}Yb_{0.20}F_4$, heat-treated at 650 °C. In addition, the standard diffraction pattern of cubic $NaTbF_4$ is also included for comparison. Magnified XRD peaks in the inset of un-doped and Yb^{3+}–Eu^{3+} co-doped nGCs show a shift related to the doping level.

It should be noted that 95SiO_2–5$NaTbF_4$ and 95SiO_2–5$NaTb_{0.98}Eu_{0.02}F_4$ nGCs present similar XRD patterns, due to their similar ionic radii ($r_{Tb^{3+}}$ = 1.040 Å, $r_{Eu^{3+}}$ = 1.066 Å) and a low doping level. However, when doping with high amounts of Yb^{3+} ions, *i.e.* nGC with composition 95SiO_2–5$NaTb_{0.78}Eu_{0.02}Yb_{0.20}F_4$, lattice constants shrink due to their smaller ionic radii when compared with Tb^{3+} ions ($r_{Yb^{3+}}$ = 0.985 Å) and a shifting of diffraction peaks towards higher angles is observed (see the inset in Fig. 1), leading to consider that dopant ions have been successfully incorporated into the crystal lattice of the $NaTbF_4$ host substituting the Tb^{3+} sites.

Additionally, morphological and microstructural information can be obtained from TEM and HRTEM images. In the TEM image of nGC with composition 95SiO_2–5$NaTb_{0.78}Eu_{0.02}Yb_{0.20}F_4$ (see Fig. 2(a)), a series of spherical nanoparticles homogeneously dispersed with a size distribution according to histogram included in the inset are observed, associated with the crystalline phase on the glassy background. The average nanoparticle size (around 23 nm) presents a good agreement with that previously obtained from the XRD.

Moreover, the HRTEM image (Fig. 2(b)) shows the detailed lattice structure of precipitated $NaTbF_4$ nanoparticles, which is indicative of the high degree of crystallinity. The atomic planes can be clearly distinguished, with a spacing of 3.189 Å, which is in good agreement with the expected value for the (111) plane of the cubic phase of $NaTbF_4$ using the Bragg equation. The power spectrum, obtained from this nanoparticle using Fourier transform (FFT) also confirms the presence of the cubic (200) and (111) planes. The corresponding filtered image is also included in the inset of Fig. 2(b).

Additionally, in order to evaluate the elemental distribution in the nGC, EDS spectra from a single NC and from the glass matrix were recorded (see Fig. 3). Cu and C peaks (originating from the support grid) were observed in both spectra. The EDS spectrum containing the nanocrystalline domain shows signals from Si and O elements along with Na, Tb, Yb and F, whereas in the EDS spectrum corresponding to the glass matrix, the intensities corresponding to these last elements were much weaker (~20 times) while the Si and O ones were more intense. The atomic ratios of Na/Tb/Yb/F were 1.04/0.78/0.20/4.03, in good agreement with the theoretical atomic ratio (1 : 1 : 4) in $NaTbF_4$.

3.2 Luminescence

The spectroscopic study is based on excitation and emission spectra, along with time-resolved PL measurements. In this sense, Fig. 4(a) shows the excitation spectrum, detecting Tb^{3+} ions at 542 nm ($^5D_4 \rightarrow {}^7F_5$ transition) of undoped nGC with composition 95SiO_2–5$NaTbF_4$, where a group of narrow and intense peaks characteristic of Tb^{3+} ions is observed in the UV-violet range between 280 and 375 nm. This is associated with

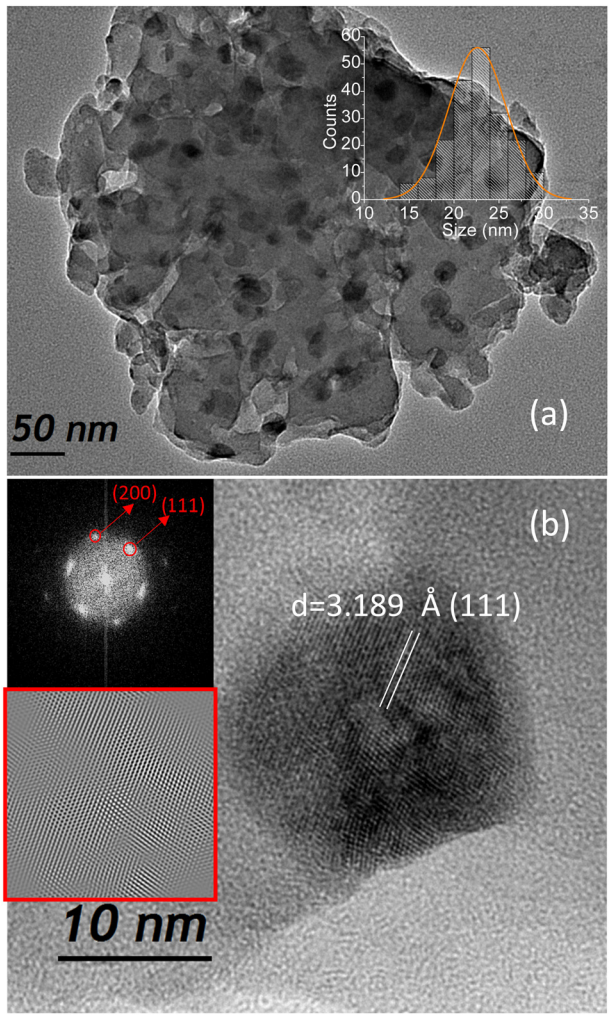

Fig. 2 (a) TEM image of nGC with composition $95SiO_2$–$5NaTb_{0.78}Eu_{0.02}$-$Yb_{0.20}F_4$ and corresponding size distribution. (b) Corresponding HRTEM image with the power spectrum (FFT) pattern and filtered higher-contrasted image of a nanoparticle.

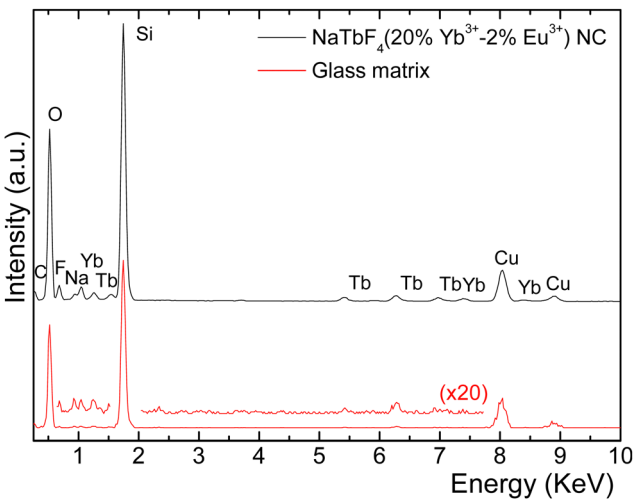

Fig. 3 EDS analysis of nGC with composition $95SiO_2$–$5NaTb_{0.78}Yb_{0.20}Eu_{0.02}F_4$ from a single NC and from an area containing the glass matrix.

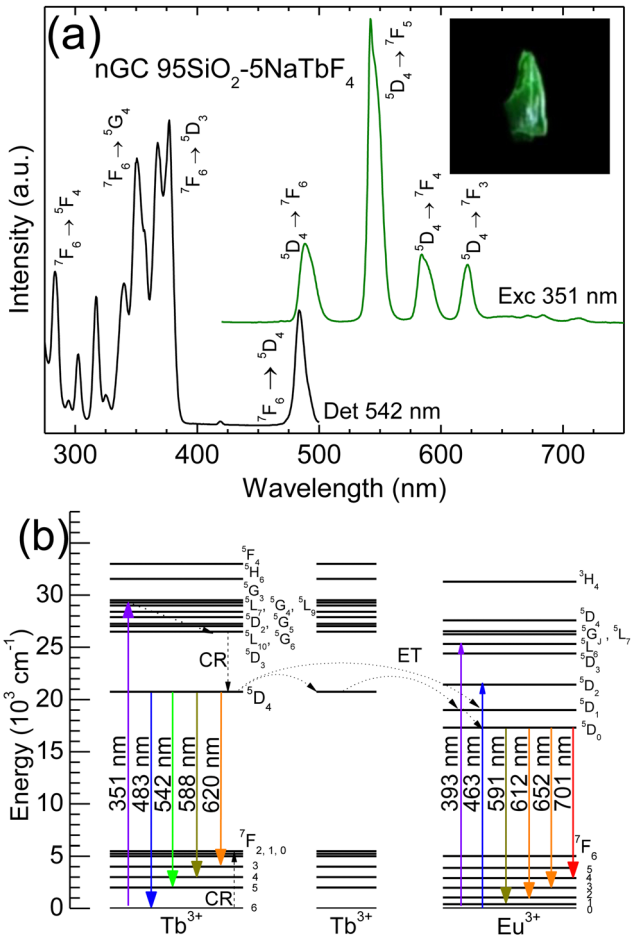

Fig. 4 (a) Excitation spectrum, detecting at 542 nm ($^5D_4 \rightarrow {}^7F_5$ transition of Tb^{3+} ions) along with emission spectrum, exciting at 351 nm ($^7F_6 \rightarrow {}^5G_4$ transition of Tb^{3+} ions) in nGC with composition $95SiO_2$–$5NaTbF_4$. (b) Energy level diagrams of Tb^{3+} and Eu^{3+} ions, along with the energy transfer mechanism.

transitions from the fundamental level $^7F_6$ to the indicated excited levels (see the energy level diagram of Tb^{3+} ions in Fig. 4(b)). In addition, a lower intensity peak associated with the $^7F_6 \rightarrow {}^5D_4$ transition is also observed, at around 483 nm.

The corresponding emission spectrum exciting Tb^{3+} ions at 351 nm ($^7F_6 \rightarrow {}^5G_4$ transition) (see Fig. 4(a)) shows peaks associated with the transitions of Tb^{3+} ions from the $^5D_4$ to the $^7F_{6,5,4,3}$ levels, where the transition at 542 nm ($^5D_4 \rightarrow {}^7F_5$) is the most intense, yielding the green color observable with the naked eye (see inset in Fig. 4(a)). No emissions from the $^5D_3$ level of Tb^{3+} ions are observed, which can be explained by the cross-relaxation processes between the Tb^{3+} ions through the known $^5D_3 + {}^7F_6 \rightarrow {}^5D_4 + {}^7F_0$ mechanism (see Fig. 4(b)) due to the high percentage of Tb^{3+} ions in $NaTbF_4$ NCs.[38]

In order to obtain Tb^{3+} sensitized Eu^{3+} red emissions, nGC with composition $95SiO_2$–$5NaTb_{0.98}Eu_{0.02}F_4$ was obtained and its luminescence features were studied. Fig. 5(a) shows excitation spectra detecting at 542 and 701 nm, corresponding to transitions $^5D_4 \rightarrow {}^7F_5$ and $^5D_0 \rightarrow {}^7F_4$ of Tb^{3+} and Eu^{3+} ions, respectively (see energy level diagram in Fig. 4(b)). We can see

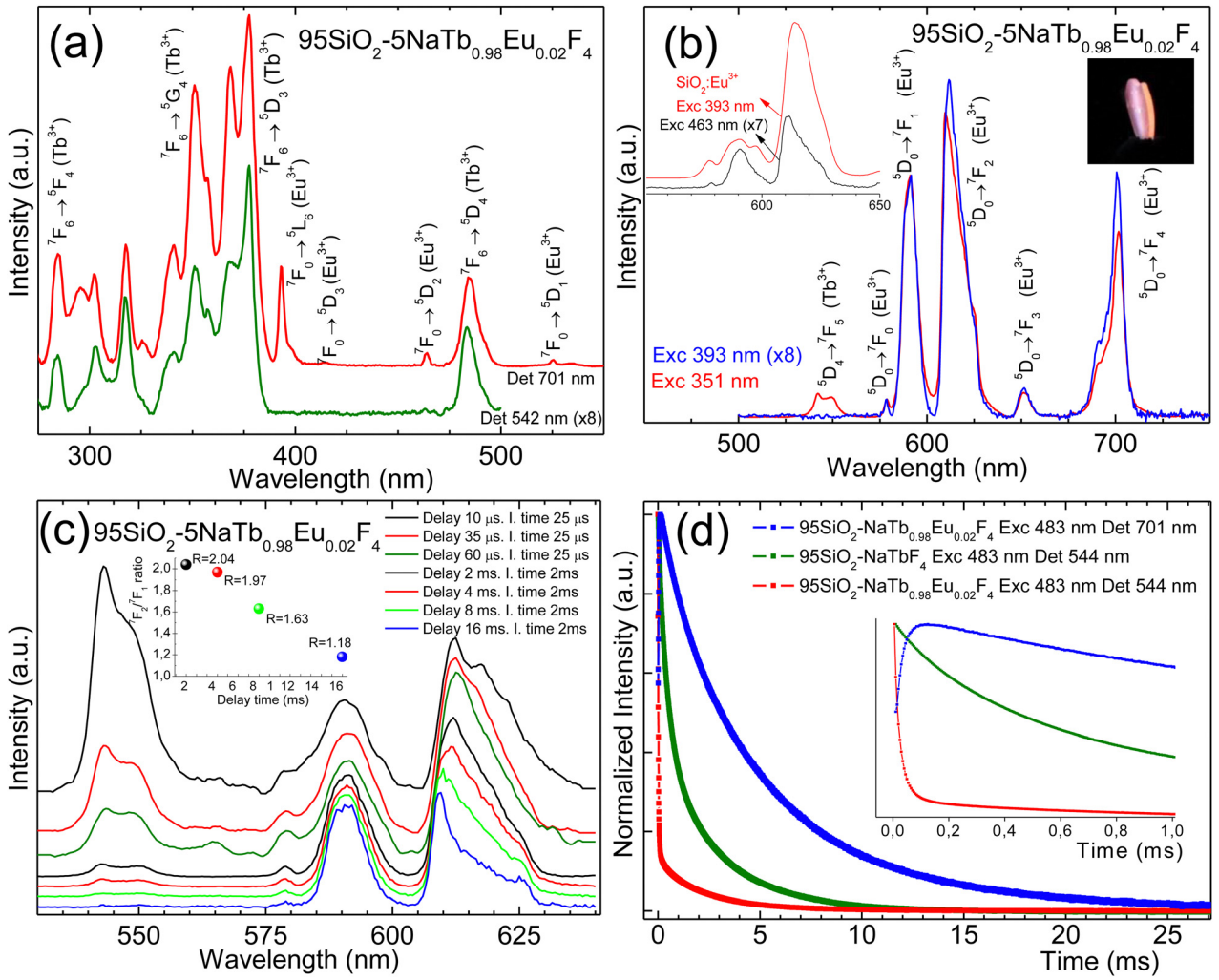

Fig. 5 (a). Excitation spectra of the nGC with composition $95SiO_2–5NaTb_{0.98}Eu_{0.02}F_4$, detecting at 542 and 701 nm, corresponding to the $^5D_4 \rightarrow {}^7F_5$ and $^5D_0 \rightarrow {}^7F_4$ transitions of Tb^{3+} and Eu^{3+} ions, respectively. Spectra have been normalized to the $^7F_6 \rightarrow {}^5D_4$ transition of Tb^{3+} ions. (b) Emission spectra exciting at 351 and 393 nm, corresponding to the $^7F_6 \rightarrow {}^5G_4$ and $^7F_0 \rightarrow {}^5L_6$ transitions of Tb^{3+} and Eu^{3+}, respectively. Spectra have been normalized to the $^5D_0 \rightarrow {}^7F_1$ transition of Eu^{3+} ions. Right inset shows a digital photograph of the spectra exciting at 351 nm. Left inset shows, emission spectra for nGC exciting Eu^{3+} ions at 463 nm and for Eu^{3+}-doped glass, exciting at 393 nm. (c) Delayed emission spectra exciting at 351 nm, with indicated delay and integration times, normalized at $^5D_0 \rightarrow {}^7F_1$ transition of Eu^{3+} ions. Inset shows long delay asymmetry ratios. (d) Luminescence decay curves of Tb^{3+} ions in $95SiO_2–5NaTbF_4$ (exciting at 483 nm and detecting at 544 nm) and $95SiO_2–5NaTb_{0.98}Eu_{0.02}F_4$ nGCs (exciting at 483 nm and detecting at 544 and 701 nm). Inset shows a magnification at short decay times.

that the excitation spectrum detecting Tb^{3+} ions consists of a series of narrow peaks, similar to those observed in the case of undoped nGC (see Fig. 4(a)), but with much less intensity (×7.5). Likewise, it is also observed that the peaks between 325 and 375 nm are relatively less intense (see Fig. 4(a)). All these would indicate that the Tb^{3+} ions involved in these transitions are located in different environments, as will be discussed later. On the other hand, when detecting Eu^{3+} ions, in addition to the Eu^{3+} characteristic excitation peaks due to transitions from the fundamental level $^7F_0$ to the indicated excited levels (see energy level diagram of Eu^{3+} ions in Fig. 4(b)), much more intense peaks corresponding to Tb^{3+} ions are also observed (×8), which is indicative of a very efficient ET mechanism from Tb^{3+} to Eu^{3+} ions.[39,40]

The corresponding emission spectra are studied by excitation at different wavelengths (see Fig. 5(b)). When exciting Eu^{3+} ions at 393 nm ($^7F_0 \rightarrow {}^5L_6$ transition), the characteristic emissions of the Eu^{3+} ions at 591, 612, 652, and 701 nm, assigned to $^5D_0 \rightarrow {}^7F_{J=1,2,3,4}$ transitions are observed according to the energy level diagram shown in Fig. 4(b). On the other hand, when exciting Tb^{3+} ions at 351 nm, where Eu^{3+} ions cannot be activated, much more intense overall emission (×8) is observed, where the predominant peaks correspond to Eu^{3+} ions, see the corresponding photograph in the right inset in Fig. 5(b), while those corresponding to Tb^{3+} ions practically disappear, confirming the efficient ET from Tb^{3+} to Eu^{3+} ions, as shown in the energy level diagrams of Fig. 4(b). The corresponding PLQY (ϕ), both for un-doped and for Eu^{3+}-

doped nGCs were recorded by an integrating sphere, giving rise to values of 59.3% and 54.4%, respectively, similar to those obtained in LaF_3:Tb^{3+}–Eu^{3+} co-doped sol–gel nGCs by N. Pawlik *et al.*[41] and in Sr_2GdF_7:Tb^{3+}-doped nGCs by L. M. Teng *et al.*[42]

Next, in order to study the local environment of the Eu^{3+} ions, their luminescence characteristics as a spectroscopic probe were considered. Thus, the asymmetry ratio R defined as the ratio between the $^5D_0 \rightarrow {}^7F_2$ and $^5D_0 \rightarrow {}^7F_1$ transitions[43] (very sensitive and insensitive to the symmetry of the local environment of the Eu^{3+} ions, respectively), presents values of 1.93 and 1.74, when Eu^{3+} ions are directly excited at 393 or through Tb^{3+} ions at 351 nm, respectively. When compared to the corresponding value for Eu^{3+} ions in SiO_2 glass (R = 3.66) (see the left inset in Fig. 5(b)), these values suggest that a significant fraction of Eu^{3+} ions have been incorporated into an environment with inversion symmetry. In addition, it is also observed that when exciting Eu^{3+} ions at 463 nm ($^7F_0 \rightarrow {}^5D_2$, hypersensitive transition to the local structure around Eu^{3+} ions and therefore prohibited in environments with inversion symmetry), the emissions are much less intense, seven times, and the corresponding R value is 2.24, suggesting the presence of these Eu^{3+} on the surface of $NaTbF_4$ NCs or remnants in the glassy environment, see the left inset in Fig. 5(b).

Additionally, in order to further analyse the ET mechanisms from Tb^{3+} to Eu^{3+} ions, time-resolved luminescence measurements were carried out. Time-resolved emission spectra exciting Tb^{3+} ions at 351 nm with different delays up to 16 ms are shown in Fig. 5(c). For different delays, the emission lines are at the same position but present slightly different shapes, suggesting different luminescent sites in the nGCs for both Tb^{3+} and Eu^{3+} ions. It can be observed that quenching of Tb^{3+} emission (due to very efficient ET from Tb^{3+} to Eu^{3+} ions) is almost complete when the delay time is only 60 μs. The residual Tb^{3+} emission is probably due to Tb^{3+} ions residing on the surface of NCs or remaining in the glassy environment. On the other hand, when the delay is progressively increased, the asymmetry ratio and the sharpness of the $^5D_0 \rightarrow {}^7F_2$ transition of Eu^{3+} ions are clearly modified (see inset in Fig. 5(c)), suggesting that for long delays, the contribution of Eu^{3+} ions hosting in the $NaTbF_4$ nanocrystalline environments become more important.

To support this assumption, measurements of transient evolution of the luminescence corresponding to Tb^{3+} and Eu^{3+} ions, exciting $^7F_6 \rightarrow {}^5D_4$ transition of Tb^{3+} ions, under 6 ns pulsed 483 nm excitation (OPO) were also carried out (see Fig. 5(d)). All decay curves are not perfectly exponential, which can be associated with different activator sites in the nGCs. Thus, by fitting with biexponential decay functions, the PL lifetimes for the $^5D_4$ level of Tb^{3+} ions in undoped and Eu^{3+} doped nGCs were determined to be τ_1 = 438 μs, τ_2 = 2,9 ms and τ_1 = 23 μs, τ_2 = 2.2 ms, respectively. The reduction of both lifetimes would indicate that a very fast ET process from Tb^{3+} to Eu^{3+} in $NaTbF_4$ NCs and another slower between remnant ions in the glassy environment is taking place in Eu^{3+} doped nGC. The corresponding transient curve for the $^5D_0$ level of Eu^{3+} ions shows a buildup at short times, 18 μs rise time (see the inset in

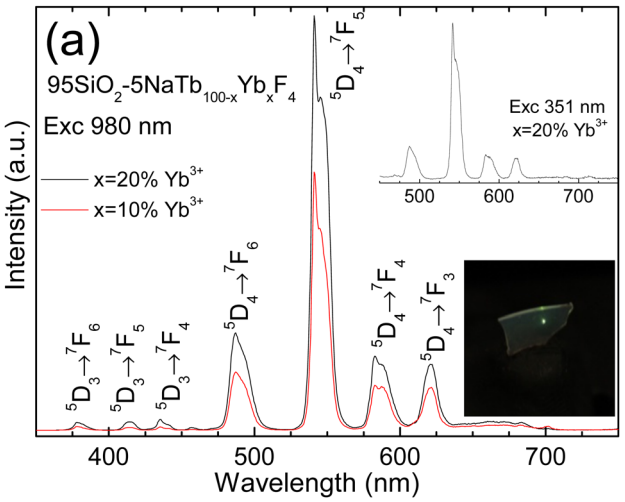

Fig. 6 Up-conversion emission spectra of nGCs with compositions $95SiO_2$–$5NaTb_{0.80}Yb_{0.20}F_4$ and $95SiO_2$–$5NaTb_{0.90}Yb_{0.10}F_4$, exciting at 980 nm and 300 mW. Inset shows the emission spectrum of the nGC with 20%Yb^{3+}, exciting at 351 nm for comparison purposes (top-side) and digital photograph, exciting at 980 nm, 300 mW (down-side).

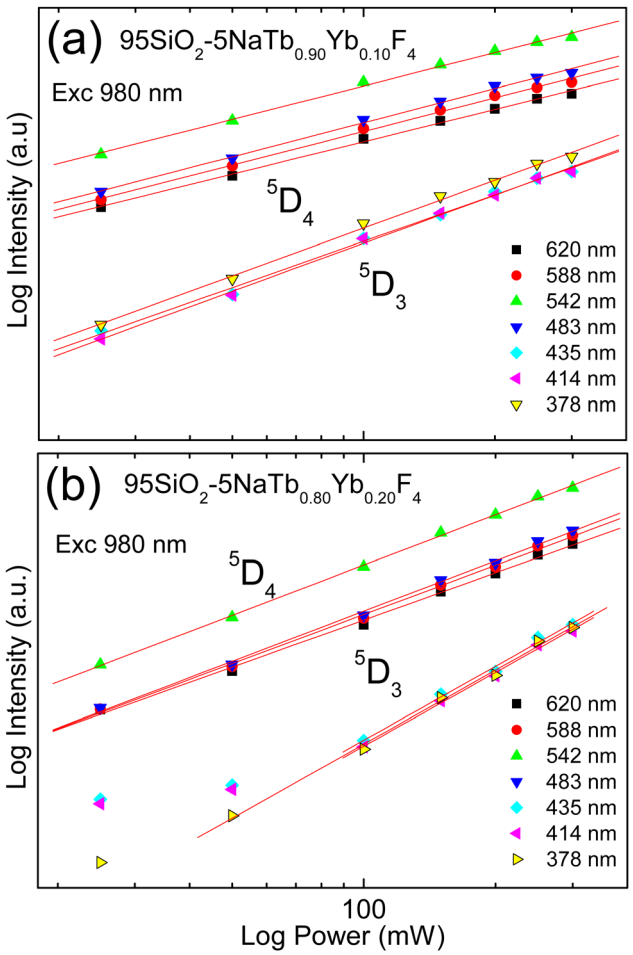

Fig. 7 Log–log plot of up-conversion intensity *versus* pump power of (a) $95SiO_2$–$5NaTb_{0.90}Yb_{0.10}F_4$, and (b) $95SiO_2$–$5NaTb_{0.80}Yb_{0.20}F_4$ nGCs, under excitation at 980 nm.

Fig. 5(d)), due to an energy migration process from Tb^{3+} to Eu^{3+} ions, followed by a biexponential decay. The PL decay lifetimes in this case were τ_1 = 6.9 ms and τ_2 = 2.7 ms, which correspond to Eu^{3+} ions in $NaTbF_4$ NCs and those remaining in the surrounding glass, respectively. The energy transfer efficiency in both environments was calculated through the expression $\eta_{ET} = 1 - \tau_s/\tau_{s0}$, where τ_s and τ_{s0} correspond to Tb^{3+} decay lifetime in the presence and absence of activator (Eu^{3+}) respectively. The values corresponding to nanocrystalline and glassy environments were 94.7% and 24.1%, respectively.

Taking into account these energy transfer efficiencies, the PLQY (ϕ) can be calculated through the well-known equation $\phi = \eta_{ET}\cdot\phi_{f-f}$ where ϕ_{f-f} represents the Eu^{3+} 4f–4f emission quantum yield, estimated by the following equation[44]

$$\phi_{f-f} = A_{MD}\cdot n^3\cdot\tau_{obs}\cdot\left(\frac{I_{tot}}{I_{MD}}\right) \quad (1)$$

where A_{MD} being equal to 14.65 s^{-1} is the spontaneous emission probability of magnetic dipole ($^5D_0 \rightarrow {}^7F_1$) transition, n is the refractive index of the media (1.432 and 1.460 for nanocrystalline and glassy environments[45–47]), τ_{obs} are Eu^{3+} decay lifetimes previously described and (I_{tot}/I_{MD}) is the ratio of the total integrated emission intensity from $^5D_0 \rightarrow {}^7F_J$ levels to the integrated intensity of the $^5D_0 \rightarrow {}^7F_1$ transition, obtained from emission spectra exciting at 351 nm with 16 ms of delay and exciting at 463 nm (partially shown in Fig. 5(c) and in left inset of Fig. 5(b)) for nanocrystalline and glassy environments, respectively. Thus, a value of 52.9% has been estimated in the Eu^{3+}-doped nGC, in good agreement with that previously recorded with an integrating sphere, 54.4%, which also confirms the ET mechanism previously proposed.

Table 1 Corresponding numbers of photons observed (n) from linear fits in log–log plots of UC emissions *versus* pump power, at indicated wavelengths and compositions

$\lambda_{emission}$ (nm)	n (10%Yb^{3+})	n (20%Yb^{3+})	n (20%Yb^{3+}–2%Eu^{3+})
378 $^5D_3 \rightarrow {}^7F_6$ (Tb^{3+})	2.39	2.97	2.69
414 $^5D_3 \rightarrow {}^7F_5$ (Tb^{3+})	2.48	2.92	3.03
435 $^5D_3 \rightarrow {}^7F_4$ (Tb^{3+})	2.44	2.76	2.75
486 $^5D_4 \rightarrow {}^7F_6$ (Tb^{3+})	1.84	2.26	2.61
541 $^5D_4 \rightarrow {}^7F_5$ (Tb^{3+})	1.81	2.21	2.39
583 $^5D_4 \rightarrow {}^7F_4$ (Tb^{3+})	1.81	2.24	—
620 $^5D_4 \rightarrow {}^7F_3$ (Tb^{3+})	1.76	2.19	—
591 $^5D_0 \rightarrow {}^7F_1$ (Eu^{3+})	—	—	1.86
612 $^5D_0 \rightarrow {}^7F_2$ (Eu^{3+})	—	—	1.89
651 $^5D_0 \rightarrow {}^7F_3$ (Eu^{3+})	—	—	1.76
701 $^5D_0 \rightarrow {}^7F_4$ (Eu^{3+})	—	—	1.87

Once DS emissions have been studied in undoped and Eu^{3+}-doped nGCs, we next study UC emissions of nGCs with compositions $95SiO_2$–$5NaTb_{0.80}Yb_{0.20}F_4$ and $95SiO_2$–$5NaTb_{0.90}Yb_{0.10}F_4$, exciting at 980 nm and 300 mW pump power (see Fig. 6). In both spectra, emission peaks associated with the $^5D_4 \rightarrow {}^7F_{J=6,5,4,3}$ transitions of Tb^{3+} ions are observed, being more intense for 20%Yb^{3+} doped nGC (×1.7), see the digital photograph in the down-side inset in Fig. 6. Moreover, three much lower intensity peaks associated with the $^5D_3 \rightarrow {}^7F_{J=6,5,4}$ transitions are also observed, whose intensities also increase when the Yb^{3+} concentration varies from 10 to 20% (×3). These enhanced intensities, both from $^5D_4$ and $^5D_3$ emissions, can be related with the increase of photons absorbed in the infrared range. Moreover, an emission spectrum exciting Tb^{3+} ions at 351 nm of nGC with 20% Yb^{3+} ions is also included in the top inset of Fig. 6, showing emissions coming from the $^5D_4$ level with similar features.

In order to analyse the nature of the UC processes in these nGCs, the number of required infrared photons to populate the different Tb^{3+} excited levels are studied by the UC intensity dependence as a function of pump power. It is known that the intensity (I) of the UC emissions is proportional to the nth power of the infrared exciting pump power (P), $I \propto P^n$, where n is the number of infrared photons absorbed for each up-conversion photon emitted. Thus, from a log–log plot of UC emission *versus* the incident pump power, the n values can be obtained. Log–log plots of UC emission *versus* the incident

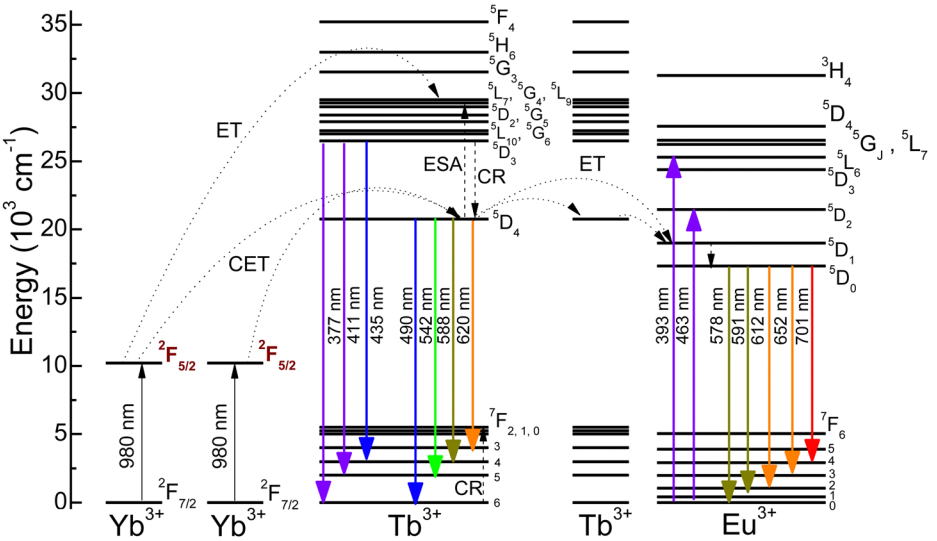

Fig. 8 Energy level diagrams of Yb^{3+}, Tb^{3+} and Eu^{3+} ions and proposed energy transfer mechanisms.

pump power for 10% and 20% Yb^{3+}-doped nGCs are shown in Fig. 7, and the corresponding n values are included in Table 1. For the 10% Yb^{3+}-doped nGC, the existence of processes involving 3 and 2 photons, for $^5D_3$ and $^5D_4$ emitting levels, respectively, becomes clear. However, in the case of 20% Yb^{3+}-doped nGC, although the emissions from the $^5D_3$ level show an expected 3-photon dependence, the $^5D_4$ level emissions present characteristics of mixing with 2- and 3-photon processes.[48]

In view of these results, the proposed ET mechanism is indicated in Fig. 8. Under NIR excitation at 980 nm, it is possible to populate the $^5D_4$ level of Tb^{3+} ions through CET involving two Yb^{3+} ions that simultaneously transfer energy to a Tb^{3+} ion ($2Yb^{3+}$:$^2F_{5/2}$+ Tb^{3+}:$^7F_6 \rightarrow 2Yb^{3+}$:$^2F_{7/2}$ + Tb^{3+}:$^5D_4$). Then, electrons in the $^5D_4$ level can relax down to the lower $^7F_{J=6,5,4,3}$ levels and emit visible emissions at 483, 542, 588, and 620 nm, respectively. The rest of the UC emissions result from the following mechanism: After the excitation from the $^5D_4$ level, a third absorption step can promote the Tb^{3+} ions to the $^5D_1$ level or a neighboring level by absorption of a photon (ESA) or by ET (or both) of Yb^{3+} ions. Next, they can relax non-radiatively to the $^5D_3$ level and subsequently give rise to the emissions of the lower levels $^7F_{J=6,5,4}$ at 378, 414 and 435 nm, respectively.

Alternatively, due to the high percentage of Tb^{3+} ions in $NaTbF_4$ NCs, these ions at the $^5D_3$ level can relax to the $^5D_4$ level by multiphonon processes and by cross-relaxation mechanisms.[38]

Finally, in order to obtain UC Eu^{3+} red emissions, nGCs with composition $95SiO_2$–$5NaTb_{0.78}Eu_{0.02}Yb_{0.20}F_4$ were obtained and their luminescence properties were studied. Excitation and emission spectra detecting and exciting Tb^{3+} and Eu^{3+} ions, present similar luminescence characteristics to Eu^{3+}-doped nGC previously studied also confirming the existence of the ET mechanism from Tb^{3+} to Eu^{3+} ions (not shown).[39,40]

Additionally, by excitation at 980 nm, it is also possible to obtain Eu^{3+} emissions through CUC processes.[28] Fig. 9(a) shows the corresponding UC emission spectra up to 300 mW pump power, where intense sharp emissions from the $^5D_0$ level of Eu^{3+} ions above 575 nm are observed. It should be noted that an R value of 1.45 (obtained from 25 mW) shows that these emissions come from Eu^{3+} ions located in $NaTbF_4$ nanocrystalline environments. Additionally, much weaker emissions from $^5D_4$ and $^5D_3$ levels of Tb^{3+} ions from of Tb^{3+} ions from 350 to 575 nm are also observed.

The corresponding UCQY values for 20%Yb^{3+}-doped and 20%Yb^{3+}–2%Eu^{3+} co-doped nGCs were 8.53×10^{-3} and 10.95×10^{-3}, respectively. These values are comparable to cubic Yb/Er-*co*-doped $NaLuF_4$ nGC[19] with UCQY around 60×10^{-3}, despite the knowledge that cooperative UC processes are several orders of magnitude less efficient than the energy transfer up-conversion (ETU) process.

In order to analyze the nature of the UC processes, the number of infrared photons (n) required to populate different excited levels as a function of the pump power is also calculated from the log–log plot (see Fig. 9(b)). The corresponding results are shown in the right column of Table 1 being consistent with those obtained for the nGC with the composition $95SiO_2$–$5NaTb_{0.80}Yb_{0.20}F_4$. Thus, emissions from $^5D_3$ and $^5D_4$ levels involve 3 and 2–3 photons, respectively (as previously discussed), while in the case of emissions from the $^5D_0$ level of Eu^{3+} ions, they are clearly associated with 2-photon processes (see the energy level diagram in Fig. 8).

Based on these results, one can propose the same ET mechanism previously described for ET from Yb^{3+} to Tb^{3+} ions, including energy migration through Tb^{3+} ions to the Eu^{3+} ones. The longer rise time of Eu^{3+} ions (270 μs) under 980 nm excitation in this case would support this assumption (see the inset in Fig. 9(a)). Thus, after the cooperative process involving two photons, it is possible to transfer energy non-radiatively towards the $^5D_1$ level of the Eu^{3+} ions. From there, after a non-radiative decay process to the $^5D_0$ level, the UC emissions in the red range dominate the spectrum originated, see the digital photograph in Fig. 9(b). Finally, it is important to note that,

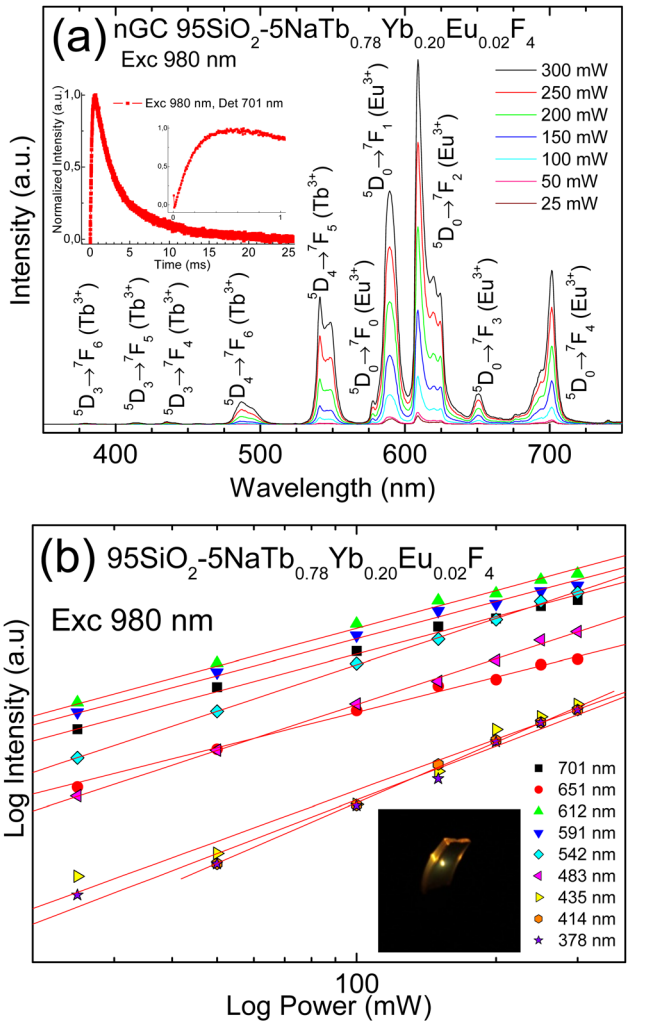

Fig. 9 (a) Up-conversion emission spectra of nGC with composition $95SiO_2$–$5NaTb_{0.78}Yb_{0.20}Eu_{0.02}F_4$, excited at 980 nm, at different pump powers up to 300 mW. Inset shows luminescence decay, exciting Yb^{3+} ions at 980 nm and detecting Eu^{3+} ions at 701 nm. (b) Corresponding dependence of up-conversion emissions intensity *versus* pump power, excited at 980 nm. Inset shows the digital photograph of those excited at 980 nm, 300 mW.

despite the probable energy back transfer from Tb^{3+} and Eu^{3+} ions to Yb^{3+} ones, the UC lifetimes of Eu^{3+} ions remain long enough (τ_1 = 6.1 and τ_2 = 1.5 ms) for applications that require time-gated techniques.[16]

4 Conclusions

Undoped and RE^{3+}-doped nGCs comprising $NaTbF_4$ NCs were successfully obtained by adequate treatment of precursor sol–gel glasses. Using XRD patterns, TEM images and EDS spectra, we can confirm the precipitation of cubic $NaTbF_4$ NCs, homogeneously dispersed in the silica matrix, with an average size of 20–25 nm, where Na, Tb and F are their main constituents. Additionally, by using Eu^{3+} as a spectroscopic ion probe, different luminescent environments were assigned.

Intense green and red emissions, visible to the naked eye, coming from Tb^{3+} to Eu^{3+} ions, respectively, were observed by DS (from UV-blue excitation) and by CUC (from 980 nm excitation) mechanisms, and the corresponding quantum yields were measured. Time-resolved spectra and transient evolution of luminescence evidenced an efficient energy migration from Tb^{3+} to Eu^{3+} ions, and from Yb^{3+} to Eu^{3+} ions through Tb^{3+} ones, making it possible to obtain long lived UC Eu^{3+} red emissions, which is very useful for time-gated luminescence techniques. These results allow considering these nGCs as UV/NIR to VIS converter materials for potential use in solar cells, w-LEDs and in anti-counterfeiting applications.

Conflicts of interest

There are no conflicts to declare.

Acknowledgements

This work has been financially supported by "Vicerrectorado de Investigación, Transferencia y Campus Santa Cruz y Sur", University of La Laguna NACSOS-project (1189_2020), MAGEC-REEsearch project (ProID2017010078) of "Agencia Canaria de Investigación" (ACIISI) and by Gobierno de Canarias (Proyecto "Tierras raras", Grant number SD-22/25). The authors would also like to thank the SEGAI-ULL for providing XRD, TEM and EDS measurement facilities.

Notes and references

1 T. T. Basiev, I. T. Basieva and M. E. Doroshenko, *J. Lumin.*, 2013, **133**, 233–243.
2 A. A. Lyapin, P. P. Fedorov, E. A. Garibin, A. V. Malov, V. V. Osiko, P. A. Ryabochkina and S. N. Ushakov, *Opt. Mater.*, 2013, **35**, 1859–1864.
3 X. Li, D. Chen, F. Huang, G. Chang, J. Zhao, X. Qiao, X. Xu, J. Du and M. Yin., *Laser Photonics Rev.*, 2018, **12**(7), 1800030–1800037.
4 E. N. Afshar, *Mod. Phys. Lett. B*, 2015, **29**, 1550118–1550126.
5 J. J. Velázquez, V. D. Rodríguez, A. C. Yanes, J. del-Castillo and J. Méndez-Ramos., *Opt. Mater.*, 2012, **34**, 1994–1997.
6 J. J. Velázquez, V. D. Rodríguez, A. C. Yanes, J. del-Castillo and J. Méndez-Ramos., *J. Appl. Physiol.*, 2010, **108**, 113530–113535.
7 A. C. Yanes and J. del-Castillo., *J. Alloys Compd.*, 2016, **658**, 170–176.
8 X. Li, C. Yang, L. Qiu, S. Wang, Y. Chen, M. Yin and D. Chen., *Laser Photonics Rev.*, 2022, **16**(1), 2100346–2100359.
9 V. Harish, D. Tewari, M. Gaur, A. Bihari Yadav, S. Swaroop, M. Bechelany and A. Barhoum., *Nanomaterials*, 2022, **12**, 457.
10 G. Liang, H. Wang, H. Shi, H. Wang, M. Zhu, A. Jing, J. Li and G. Li., *J. Nanobiotechnol.*, 2020, **18**, 154–175.
11 Y. Yang, L. Wang, B. Wan, Y. Gu and X. Li., *Front. Biotechnol.*, 2019, **7**, 320–323.
12 S. Siddique and J. C. L. Chow, *Nanomaterials*, 2020, **10**, 1700–1739.
13 S. Hao, G. Chen and C. Yang, *Theranostics*, 2013, **3**, 331–345.
14 X. Wang, Q. Liu, Y. Bu, C.-S. Liu, T. Liu and X. Yan., *RSC Adv.*, 2015, **5**, 86219–86236.
15 W. Ren, G. C. Clarke, J. Zhou and D. Jin., *Adv. Mater.*, 2020, **32**, 1901430–1901444.
16 H. Suo, Q. Zhu, X. Zhang, B. Chen, J. Chen and F. Wang., *Mater. Today Phys.*, 2021, **21**, 100520–100529.
17 S. Torres-García, C. Hernández-Álvarez, M. Medina-Alayón, P. Acosta-Mora, A. C. Yanes, J. del-Castillo, A. Menéndez-Velázquez and J. Méndez-Ramos., *Ceram. Int.*, 2022, DOI: 10.1016/j.ceramint.2022.09.307.
18 S. Wang, J. Zhu, Y. He, Z. Li, J. Lin, S. Liao, F. Huang, P. Huang, Y. Zheng, X. Li and D. Chen., *Laser Photonics Rev.*, 2022, **16**(8), 2200039–2200046.
19 S. Wang, J. Lin, X. Li, J. Chen, C. Yang, P. Huang, Y. Cheng and D. Chen., *J. Mater. Chem. C*, 2020, **8**, 16151–16159.
20 J. del-Castillo, J. Méndez-Ramos, P. Acosta-Mora and A. C. Yanes., *J. Lumin.*, 2022, **241**, 118490–118494.
21 T. Parangi and M. K. Mishra, *Comments Inorg. Chem.*, 2019, **0**, 1–37.
22 E. D. Zanotto, *Am. Ceram. Soc. Bull.*, 2010, **89**(8), 19–27.
23 J. del-Castillo and A. C. Yanes., *Phys. Chem. Chem. Phys.*, 2018, **20**, 20910–20918.
24 C. Wang, T. Zhou, J. Jiang, H. Geng, Z. Ning, X. Lai, J. Bi and D. Ga., *ACS Appl. Mater. Interfaces*, 2017, **9**(31), 26184–26190.
25 B. Yu, B. Zheng, H. Xia, J. Wang, H. Song and B. Chen., *Ceram. Interfaces*, 2021, **47**, 9668–9678.
26 A. C. Yanes, J. del-Castillo, D. Luis and J. Puentes., *J. Lumin.*, 2016, **170**, 789–794.
27 J. Méndez-Ramos, A. C. Yanes, A. Santana-Alonso and J. del-Castillo., *Chem. Phys. Lett.*, 2013, **555**, 196–201.
28 T. Grzyb., *RSC Adv.*, 2014, **4**, 2590–2595.
29 N. Rakov, S. C. Duarte and D. S. Maciel., *J. Lumin.*, 2019, **214**, 116561–116566.
30 Q. Han, Y. Zou, H. Wu, Y. Song, Y. Wang and X. Zhang., *J. Lumin.*, 2020, **225**, 117348–117355.
31 P. Du, W. Ran, W. Li, L. Luo and X. Huang., *J. Mater. Chem. C*, 2019, **7**, 10802–10809.

32 Y. Luo, R. Yang, X. Zhang, B. Hu, S. Hu, L. Zhou and J. Yan., *CrystEngComm*, 2015, **17**, 7762–7771.
33 Z. Chen, Z. Geng, D. Shao, Z. Zhou and Z. Wang., *CrystEngComm*, 2012, **14**, 2251–2257.
34 X. Li, X. Chen, S. Yuan, S. Liu, C. Wang and D. Chen., *J. Mater. Chem. C*, 2017, **5**, 10201–10210.
35 J. del-Castillo, A. C. Yanes, A. Santana-Alonso and J. Méndez-Ramos., *Opt. Mater.*, 2014, **37**, 511–515.
36 A. C. Yanes, P. Mirabal-Bello and J. del-Castillo., *J. Alloys Compd.*, 2021, **856**, 157183–157191.
37 X. Y. Jin, Z. Y. Wang, H. Y. Xu, M. C. Jia and Z. L. Fu. Mat., *Today Chem.*, 2022, **24**, 100771–100779.
38 R. Reisfeld and C. K. Jorgensen, *Handbook on the Physics and Chemistry of Rare Earths*, North Holland, Amsterdam, 1987.
39 R. Wang, D. Zhou, J. Qiu, Y. Yang and C. Wang., *J. Alloys Compd.*, 2015, **629**, 310–314.
40 X. Zhang, L. Zhou, Q. Pang, J. Shi. and M. Gong., *J. Phys. Chem. C*, 2014, **118**(14), 7591–7598.
41 N. Pawlik, B. Szpikowska-Sroka and W. A. Pisarski, *Materials*, 2020, **13**, 2522–2539.
42 L. M. Teng, W. Zhang, W. P. Chen, J. K. Cao, X. Y. Sun and H. Guo., *Ceram. Interfaces*, 2020, **46**, 10718–10722.
43 K. Binnenmans., *Coord. Chem. Rev.*, 2015, **295**, 1.
44 G. Lesly Jiménez, M. J. Rosales-Hoz, B. Handke, M. A. Leyva, C. Vázquez-López, I. Padilla-Rosales, C. Falcony and D. Dorosz., *J. Lumin.*, 2022, **248**, 119007–119014.
45 Z. Smara, Y. Cheroura, D. Boyer, A. Potdevin, A. Chafa, O. Ziane and R. Mahiou., *Opt. Mater.*, 2020, **104**, 109932–109942.
46 M. Toki, S. Miyashita, T. Takeuchi, S. Kanbe and A. Kochi., *J. Non-Cryst. Solids*, 1998, **100**, 479–482.
47 J. D. Mackenzie and J. Non-Cryst, *Solids*, 1982, **48**, 1–10.
48 M. Xue, X. Zhu, X. Qiu, Y. Gu, W. Feng and F. Li., *ACS Appl. Mater. Interfaces*, 2016, **8**(28), 17894–17901.